Journal of Biomedical Optics

SPIEDigitalLibrary.org/jbo

Reconstruction algorithms based on l_1-norm and l_2-norm for two imaging models of fluorescence molecular tomography: a comparative study

Huangjian Yi
Duofang Chen
Wei Li
Shouping Zhu
Xiaorui Wang
Jimin Liang
Jie Tian

SPIE

Reconstruction algorithms based on l_1-norm and l_2-norm for two imaging models of fluorescence molecular tomography: a comparative study

Huangjian Yi,[a] Duofang Chen,[a] Wei Li,[a] Shouping Zhu,[a] Xiaorui Wang,[b] Jimin Liang,[a] and Jie Tian[a,c]
[a]Xidian University, School of Life Sciences and Technology, Xi'an, Shaanxi 710071, China
[b]Xidian University, School of Technical Physics, Xi'an, Shaanxi 710071, China
[c]Chinese Academy of Sciences, Institute of Automation, Beijing 100190, China

Abstract. Fluorescence molecular tomography (FMT) is an important imaging technique of optical imaging. The major challenge of the reconstruction method for FMT is the ill-posed and underdetermined nature of the inverse problem. In past years, various regularization methods have been employed for fluorescence target reconstruction. A comparative study between the reconstruction algorithms based on l_1-norm and l_2-norm for two imaging models of FMT is presented. The first imaging model is adopted by most researchers, where the fluorescent target is of small size to mimic small tissue with fluorescent substance, as demonstrated by the early detection of a tumor. The second model is the reconstruction of distribution of the fluorescent substance in organs, which is essential to drug pharmacokinetics. Apart from numerical experiments, *in vivo* experiments were conducted on a dual-modality FMT/micro-computed tomography imaging system. The experimental results indicated that l_1-norm regularization is more suitable for reconstructing the small fluorescent target, while l_2-norm regularization performs better for the reconstruction of the distribution of fluorescent substance. [DOI: 10.1117/1.JBO.18.5.056013]

Keywords: fluorescence molecular tomography; regularization method; imaging reconstruction; early detection of tumor; drug distribution.

Paper 12780RR received Dec. 7, 2012; revised manuscript received Apr. 14, 2013; accepted for publication Apr. 22, 2013; published online May 30, 2013.

1 Introduction

Fluorescence molecular tomography (FMT) has become a promising optical imaging modality that allows studying disease noninvasively and quantitatively at the molecular level.[1–3] It can be applied to drug discovery and preclinical oncological research.[3–5] The reconstruction algorithm is crucial to recover the location of fluorophore, the fluorescence yield, and the images of the fluorescent lifetime. However, the solution to the inverse problem of FMT suffers from being ill-posed due to the diffusive behavior of light in tissue. In order to obtain meaningful and stable results, it is essential to incorporate adequate *a priori* information, such as the anatomical information provided by computed tomography (CT) or magnetic resonance imaging,[6–8] and the distribution of optical properties obtained by diffuse optical tomography (DOT).[7,9] Several multimodality FMT systems have been developed.[6–9] In the reconstruction algorithms, the regularization technique is commonly used in the form of a penalty function to improve the solution. In the early stage of research, the Tikhonov regularization, namely l_2-norm regularization, is routinely employed for the inverse problem.[10,11] However, this method tends to create an oversmooth effect and generate spurious small elements, which produce noisy background when the inverse problem is severely ill-posed. Recently, the sparsity regularization, with l_1-norm penalty function, has received considerable attention due to its good performance in FMT. In the application of early detection of a tumor, the observed biological mechanisms are generally confined to localized regions. In this case, the interested biological function is somewhat "sparse," which can be utilized as *a priori* information in the form of l_1-norm penalty.[12,13] However, for the application of reconstructing the distribution of the fluorescent dye or drugs in organs, the spatial distribution of biological activity usually occurs in a large area. As a consequence, l_1-norm regularization would be no longer suitable for this problem, while l_2-norm regularization is potentially beneficial.

In this paper, we intend to fill the gap in the existing studies to systematically show the performance of l_1-norm and l_2-norm regularization methods for the two imaging models of FMT using a fair and consistent experimental setting. The first imaging model is the reconstruction of fluorophore with small size, which is to mimic the early detection of tumor. The second model is the reconstruction of the distribution of fluorescent dye in organs, which is essential to drug pharmacokinetics (PK).[14] In order to evaluate the performance of the two regularization methods, apart from numerical simulation experiments, *in vivo* experiments were also performed. A homemade dual-modality FMT/micro-computed tomography (micro-CT) imaging system is used as the experimental setup.

The outline of this paper is as follows. In Sec. 2, the methods, models, and system setup are detailed. In Sec. 3, the simulation and *in vivo* experiments are shown, and the results are described. Finally, we discuss and make conclusions of this paper.

Address all correspondence to: Jimin Liang, Xidian University, School of Life Sciences and Technology, 266 Xinglong Section of Xifeng Road, Xi'an, Shaanxi 710126, China. Tel: +86 29 81891070; Fax: +86 29 81891060; E-mail: jimleung@mail.xidian.edu.cn

0091-3286/2013/$25.00

2 Methodologies

2.1 *Establishment of the System Equation*

Since practical FMT operates in the wavelength range of the near-infrared, scattering predominates in the light–matter interaction as light propagates through biological tissues.[15] The diffusion equation is sufficiently accurate for the light propagation.[16,17] Here, we only reconstructed the fluorophore distribution in the tissue and the optical properties are known *a priori*. The Robin boundary condition is performed on the boundary.[18] When FMT is excited by a continuous wave point source, the coupled diffusion equations can be presented as follows:

$$\begin{cases} \nabla \cdot [D_x(r)\nabla\Phi_x(r)] - \mu_{ax}(r)\Phi_x(r) = -\Theta\delta(r - r_S) \\ \nabla \cdot [D_m(r)\nabla\Phi_m(r)] - \mu_{am}(r)\Phi_m(r) = -\Phi_x(r)\eta\mu_{af}(r) \end{cases}, \tag{1}$$

where $r \in \Omega$, Ω is the domain under consideration. The subscripts x and m denote excitation light and emission light, respectively. $D_{x,m} = 1/3[\mu_{ax,am} + (1-g)\mu_{sx,sm}]$ is the diffusion coefficient with $\mu_{sx,sm}$ as the scattering coefficient, g is the anisotropy parameter, and $\mu_{ax,am}$ is the absorption coefficient. $\Phi_{x,m}$ denotes the photon density. The fluorescent yield $\eta\mu_{af}$ is the unknown parameter to be reconstructed, which is denoted as $X(r)$ hereafter. Using a finite element method to solve Eq. (1), we obtained the following matrix forms:[19–21]

$$K_x\Phi_x = b_x, \tag{2}$$

$$K_m\Phi_m = FX, \tag{3}$$

where $K_{x,m}$ is the system matrix. F is obtained by discretizing the unknown fluorescent yield distribution. For total S excitation point sources, we have the final weighted matrix

$$\Phi_m = AX. \tag{4}$$

This is a relationship between the measurements Φ_m and the desired unknown fluorophore distribution X.

It should be noted that the determination of a unique solution to Eq. (4) suffers from being ill-posed. A proper regularization method is necessary for finding a unique and stable solution. In general, Eq. (4) can be solved by the following minimization problem with the l_p regularization term:

$$\min_X\{\|AX - \Phi_m\|_2^2 + \lambda_p\|X\|_p\}, \tag{5}$$

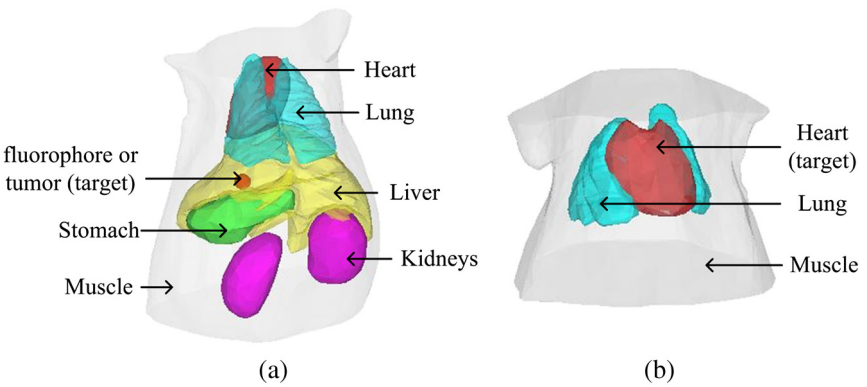

Fig. 1 Imaging models. (a) Model A: reconstruction of small fluorophore. (b) Model B: reconstruction of fluorescent dye distribution in organs, the heart as exemplar.

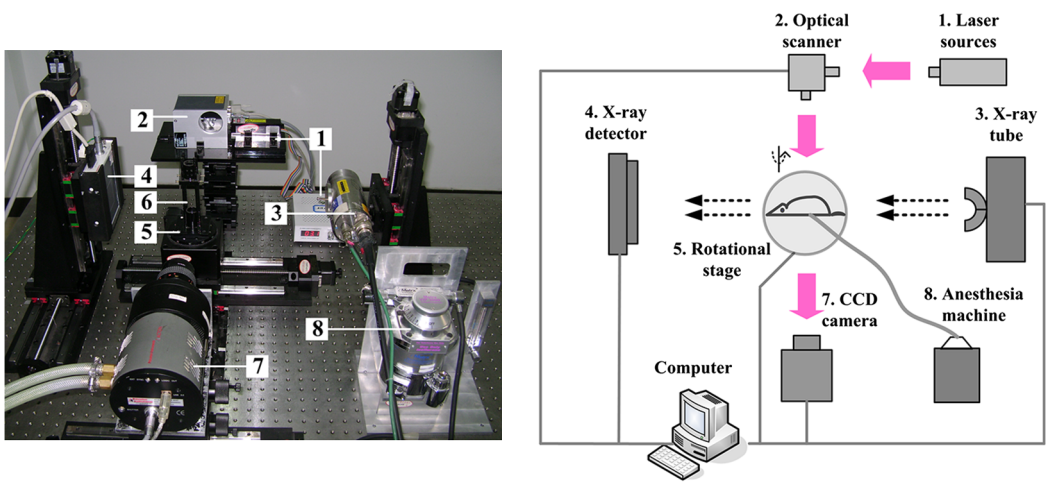

Fig. 2 (a) Dual-modality FMT/micro-CT imaging system. (1) Laser. (2) Optical scanner. (3) X-ray tube. (4) X-ray detector. (5) Rotational stage. (6) Mouse holder. (7) CCD camera. (8) Anesthesia machine. (b) The schematic diagram of different components of the system.

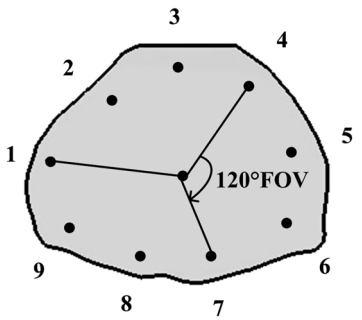

Fig. 3 The plane of excitation source. The black dots indicate the location of the isotropic point sources. For each excitation source, fluorescence is detected at the opposite side with a 120-deg field of view (FOV).

where λ_p is the regularization parameter and $\|X\|_p$ is the p-norm of X. When $p = 2$, Eq. (5) becomes the l_2-norm regularization problem, which is commonly called Tikhonov regularization. When $p = 1$, it is the l_1-norm regularization problem. The l_2-norm regularization problem can be solved efficiently using standard minimization methods, like the Newton method and the conjugate gradient method.[22] In the past years, l_1-norm regularization method has received considerable attention due to the development of a compressive sensing theory, and it can be solved by primal-dual interior-point, orthogonal matching pursuit, iterative shrinkage-thresholding, and so on.[23–35]

2.2 *Imaging Models*

Two imaging models of FMT were studied in this paper. The first imaging model is the reconstruction of fluorophore with small size, denoted as model A, which is to mimic the early detection of a tumor. Early detection of a tumor greatly increases the chances for successful treatment, and it represents one of the most promising approaches to reducing the growing tumor burden.[26] The localization of the early tumor is absolutely crucial to diagnosis and treatment. Considerable attention has been paid on the early detection of various diseases.[27–31] In the early stage of tumor, the biological mechanisms of interest are active in a very small region, which is "sparse" compared to the reconstruction region, as shown in Fig. 1(a). The second model is reconstructing the distribution of fluorescent dye in organs at a specific time point, denoted as model B, which is a part and parcel of the drug PK.[14] It is helpful in the development of drug discovery and studying disease treatment. The reconstruction of concentration of fluorescent dye distributed in organs usually occurs with a large volume, as shown in Fig. 1(b), and does not concentrate in a localized region as model A. The different characteristics of these two models motivate our investigation of a suitable reconstruction algorithm.

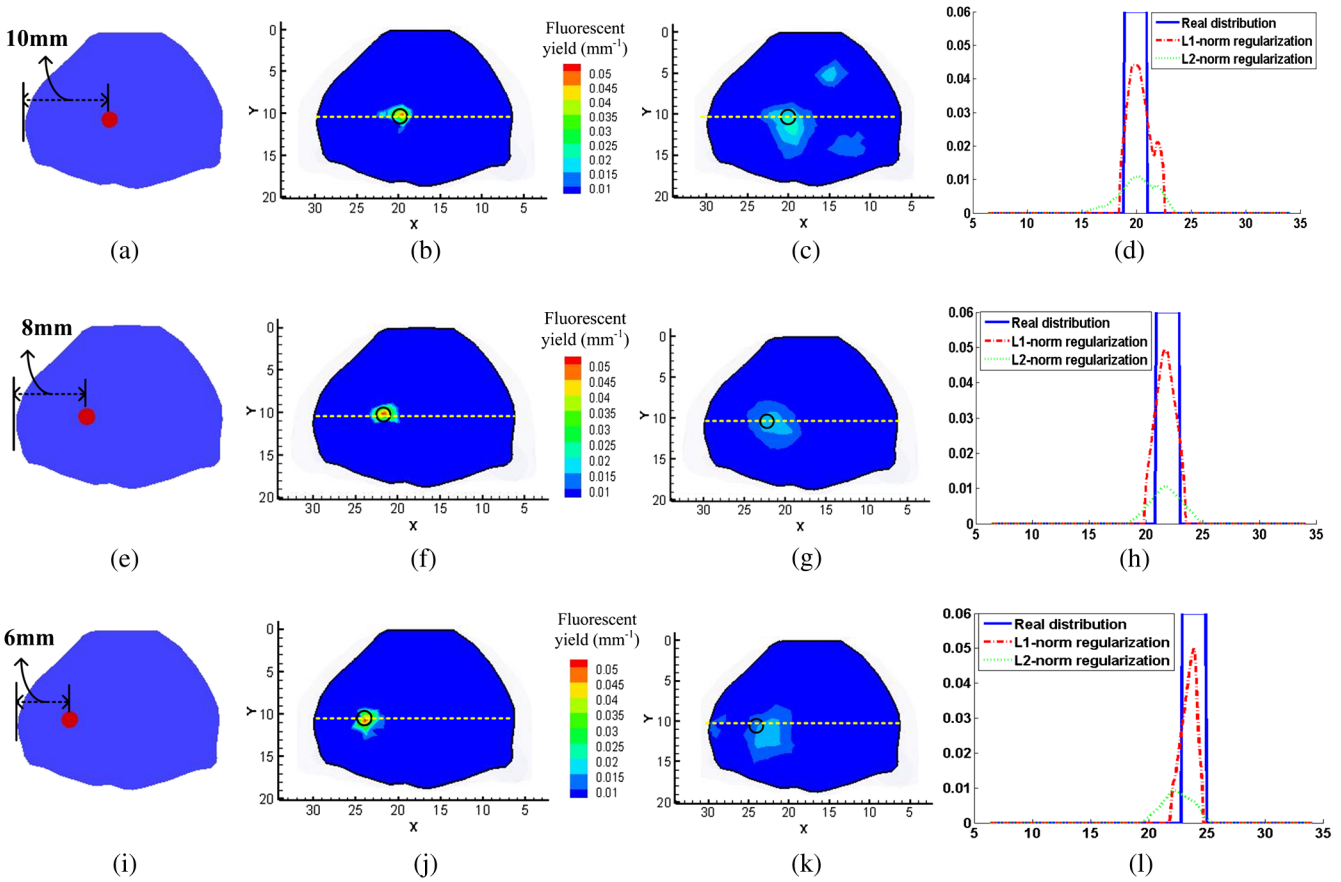

Fig. 4 Results for three different locations of fluorophore by l_1-norm and l_2-norm regularization methods. The first column are the different positions of fluorophore. The second column are the reconstructed results by l_1-norm regularization at $z = 16.5$ mm, while the third column are those by l_2-norm regularization method, with a threshold of 70% of the maximum value. The black circles in the second and third columns denote the real positions of fluorescent target. The blue solid lines in the fourth column are the real distribution along the yellow dotted lines in the second column, while the red dash dot line and green dotted line represent the reconstructed distribution by l_1-norm and l_2-norm regularization methods, respectively.

In the past years, Tikhonov regularization and sparsity regularization were developed for reconstruction based on the model of the early detection of tumor.[10,12] To the best of our knowledge, they have not been performed on model B. This further motivates us to make a comparative study of l_1-norm regularization and l_2-norm regularization methods based on the two imaging models.

2.3 *Imaging System*

We developed our prototype FMT/micro-CT dual-modality imaging system for acquiring experimental data and high-resolution anatomical information. This hybrid system, as shown in Fig. 2, avoids the issue of anatomical transmogrification of coregistration between two separate FMT and micro-CT scanners. A continuous wave laser source (CrystaLaser, Reno, Nevada, and Model No. CL671-050-O) with a power of 3 mw provides an illumination at 670 nm. The laser is a stabilized compact red laser and the spot diameter of the laser beam is approximately 0.85 mm. The target is placed on a rotational stage, which is controlled by the computer. A highly sensitive charge-coupled device (CCD) camera (Princeton Instruments PIXIS 2048B, Roper Scientific, Trenton, NJ), which is cooled to −70°C, is employed to collect fluorescence signals. A Nikon Micro-NIKKOR 55 mm $f/2.8$ manual focus lens is mounted on the CCD camera. A custom-made 35 nm band-pass filter (HZXD, Beijing, China) centered at 720 nm is used to allow light transmission at the emission wavelength of 710 nm. The axial direction of camera lens is vertical to the x-ray central projection direction. The micro-CT imaging consists of an x-ray tube (Oxford Instruments series 5000 Apogee X-ray tube, X-ray Technology Inc., CA) with a focal spot size of 35 μm and a high-resolution flat panel x-ray detector (Hamamatsu C7921CA-02, Hamamatsu city, Japan) with a 1032×1012 pixel photo diode array with a 50 μm pixel pitch. It can provide three-dimensional (3-D) anatomic information.[32] When rotating the stage to different angles, multiple view measurements can be obtained. The FMT experiments were performed in a totally dark environment. An anesthesia machine (Matrix Medical Inc., Minnesota) is employed to keep the mouse sedated during the experiment.

Table 1 Optical parameters of the mouse organs (units of μ_a and μ_s': mm^{-1}).

Tissue	μ_{ax}	μ_{sx}'	μ_{am}	μ_{sm}'
Muscle	0.0052	1.08	0.0068	1.03
Heart	0.0083	1.01	0.0104	0.99
Lungs	0.0133	1.97	0.0203	1.95
Liver	0.0329	0.70	0.0176	0.65
Kidneys	0.0660	2.25	0.0380	2.02
Stomach	0.0114	1.74	0.0070	1.36

3 Experiments and Results

In this section, l_1-norm regularization and l_2-norm regularization methods were performed on the two aforementioned imaging models of FMT, respectively. Numerical and *in vivo* experiments have been designed for testing these two methods. Here, l_1-norm regularization is solved by incomplete variables truncated conjugate gradient method, which has been demonstrated as an effective sparse regularization method in bioluminescence tomography.[33] The l_2-norm regularization problem is solved by conjugate gradient method.[22] For each experiment, the algorithm was tested using a range of regularization parameters, and the best reconstruction was selected based on visual assessment. All of the reconstructions were conducted on a personal computer with a 2.66 GHz Intel(R) Xeon(R) CPU E5430 and 8.00 GB RAM. For all the numerical experiments, the fluorescent targets were excited by nine point sources at different positions in sequence, as shown in Fig. 3. For each point source, the surface data on the opposite side with a 120-deg field of view were measurable. The fluorescent yield was set to be 0.06 mm^{-1}.

3.1 *Model A: Small Fluorophore Reconstruction*

3.1.1 *Numerical simulation*

In this section, a 3-D digital mouse model was considered and the cryosection data were utilized to provide anatomical information.[34] We supposed that there was only one small fluorophore to be detected and only the torso section of the mouse was selected as the region to be investigated, as shown in Fig. 1(a). The small sphere was to imitate the location of

Table 2 Quantitative results for the three cases by two regularization methods.

Case	Method	Real position center (mm)	Reconstructed position center (mm)	Location error (mm)	Reconstructed fluorescent yield (mm^{-1})	Relative error of yield (%)	FWHM (mm)	Time (s)
1	l_1-norm	(19.9, 10.4, 16.4)	(20.3, 9.8, 16.3)	0.73	0.050	16.7	2.3	20.9
	l_2-norm		(19.5, 11.2, 15.9)	1.02	0.015	75.0	4.0	6.63
2	l_1-norm	(21.9, 10.4, 16.4)	(21.9, 10.2, 16.6)	0.28	0.055	8.3	2.3	36.2
	l_2-norm		(21.9, 10.7, 16.9)	0.58	0.011	81.7	3.2	5.4
3	l_1-norm	(23.9, 10.4, 16.4)	(23.9, 11.2, 16.4)	0.80	0.054	10.0	1.4	32.2
	l_2-norm		(23.0, 11.1, 16.4)	1.11	0.014	76.7	3.2	1.7

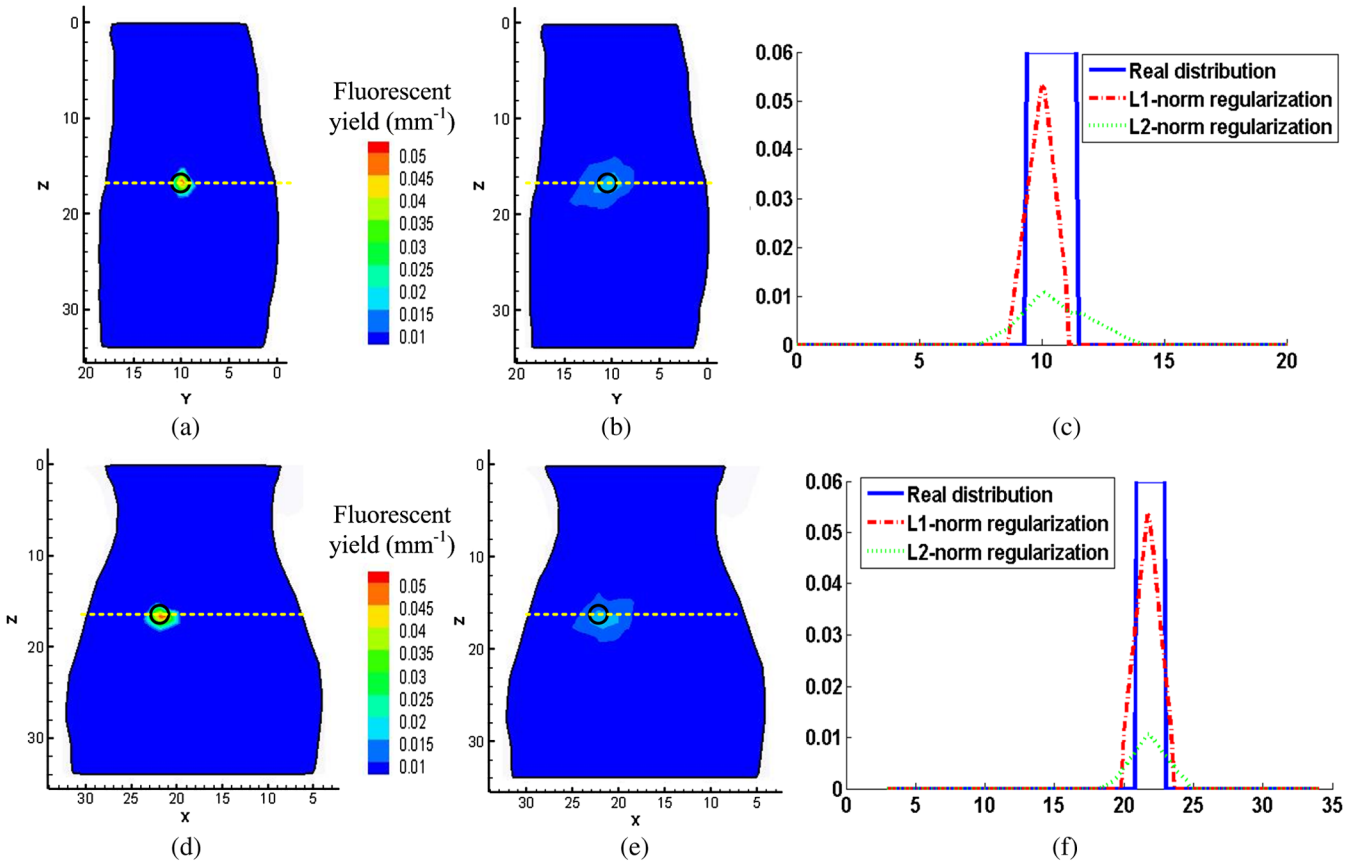

Fig. 5 Results by l_1-norm and l_2-norm regularization methods for case 2, with a threshold of 70% of the maximum value. The first column are reconstructed by l_1-norm regularization and the second column are recovered by l_2-norm regularization. (a) and (b) are coronal views; (d) and (e) are sagittal views. The black circles in (a), (b), (d), and (e) denote the real fluorophore. The blue solid lines in the third column are the real distribution along the yellow dotted lines in the first and second columns, while the red dash dot line and green dotted line represent the reconstructed distribution by l_1-norm and l_2-norm regularization methods, respectively.

fluorophore. A coarse mesh (3905 nodes and 20,380 tetrahedral-elements) was used for the inverse problem. Three different locations of fluorophore were considered, as shown in Fig. 4(a), 4(e), and 4(i). The fluorophore was positioned 10, 8, and 6 mm off the bound of the left for case 1, case 2, and case 3, respectively. The optical properties for different organs are listed in Table 1.[35,36] The second and third columns are the reconstructed results at $z = 16.5$ mm plane by l_1-norm and l_2-norm regularization methods, respectively. We defined the location error (LE) to analyze the results quantitatively.

$$LE = [(x - x_0)^2 + (y - y_0)^2 + (z - z_0)^2]^{1/2}, \qquad (6)$$

where (x_0, y_0, z_0) is the actual center of the fluorophore and (x, y, z) is the reconstructed coordinate of node with maximum reconstructed value for that fluorophore. The relative error (RE)

Table 3 Optical parameters of the mouse organs at 670 and 710 nm (units of μ_a and μ_s': mm^{-1}).

	670 nm		710 nm	
	μ_{ax}	μ_{sx}'	μ_{am}	μ_{sm}'
Muscle	0.075	0.412	0.043	0.350
Heart	0.051	0.944	0.030	0.870
Lungs	0.170	2.157	0.097	2.093
Liver	0.304	0.668	0.176	0.629
Kidneys	0.058	2.204	0.034	2.021
Stomach	0.010	1.417	0.007	1.340

Table 4 Quantitative analysis of the reconstruction results for simulation experiments of model A with different perturbation levels of optical parameters.

Perturbation	Method	Location error (mm)	Reconstructed fluorescent yield (mm^{-1})
±5%	l_1-norm	0.24 ± 0.02	0.0551 ± 0.0016
	l_2-norm	0.83 ± 0.22	0.0107 ± 0.0008
±10%	l_1-norm	0.27 ± 0.06	0.0546 ± 0.0033
	l_2-norm	0.86 ± 0.29	0.0106 ± 0.0008
±15%	l_1-norm	0.27 ± 0.07	0.0534 ± 0.0058
	l_2-norm	0.99 ± 0.34	0.0107 ± 0.0012

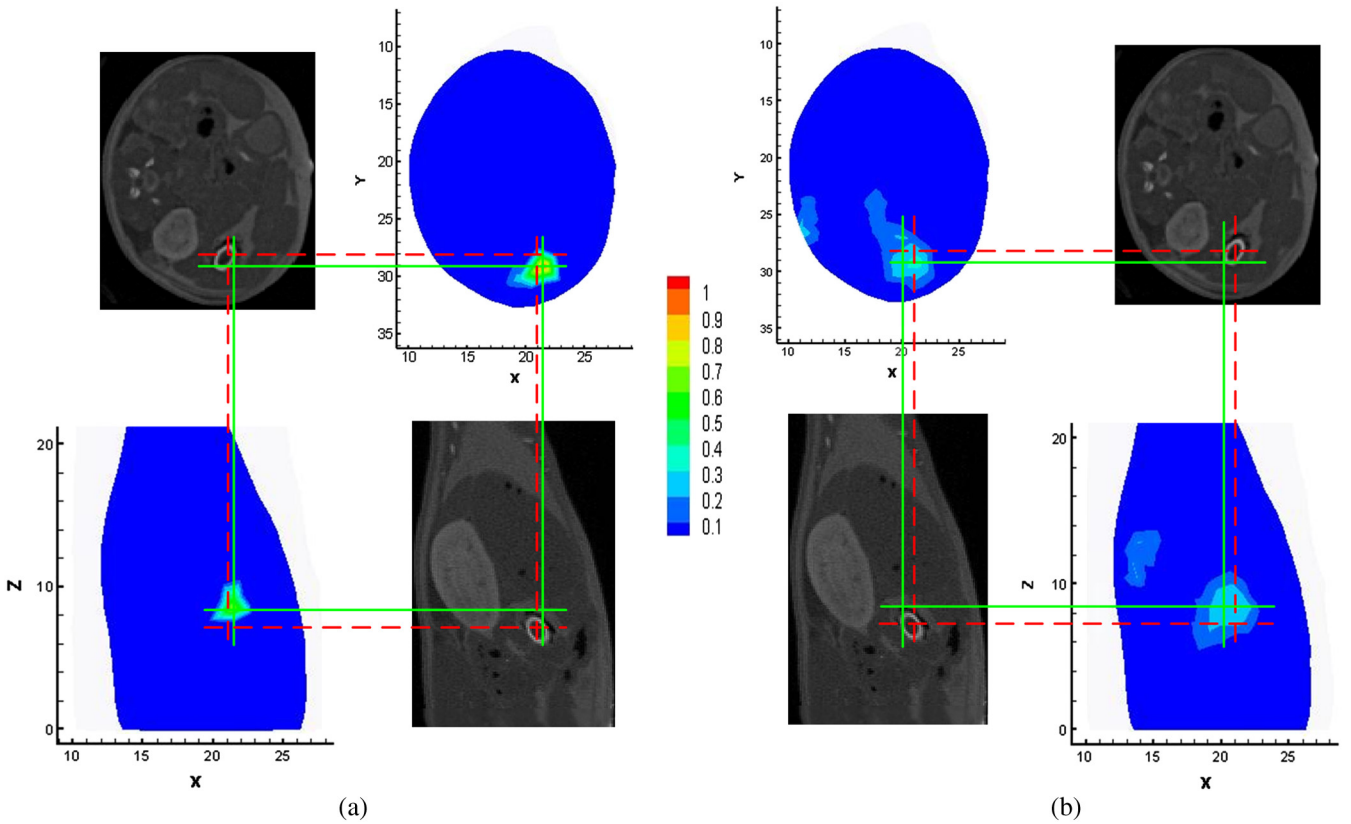

Fig. 6 Results of *in vivo* experiment for model A, with a threshold of 70% of the maximum value. The reconstructed images are normalized by the actual value of 0.0402 mm^{-1}. (a) Result of l_1-norm regularization method; (b) Result of l_2-norm regularization. The red dashed lines denote the real source center, and the green solid lines represent the reconstructed center.

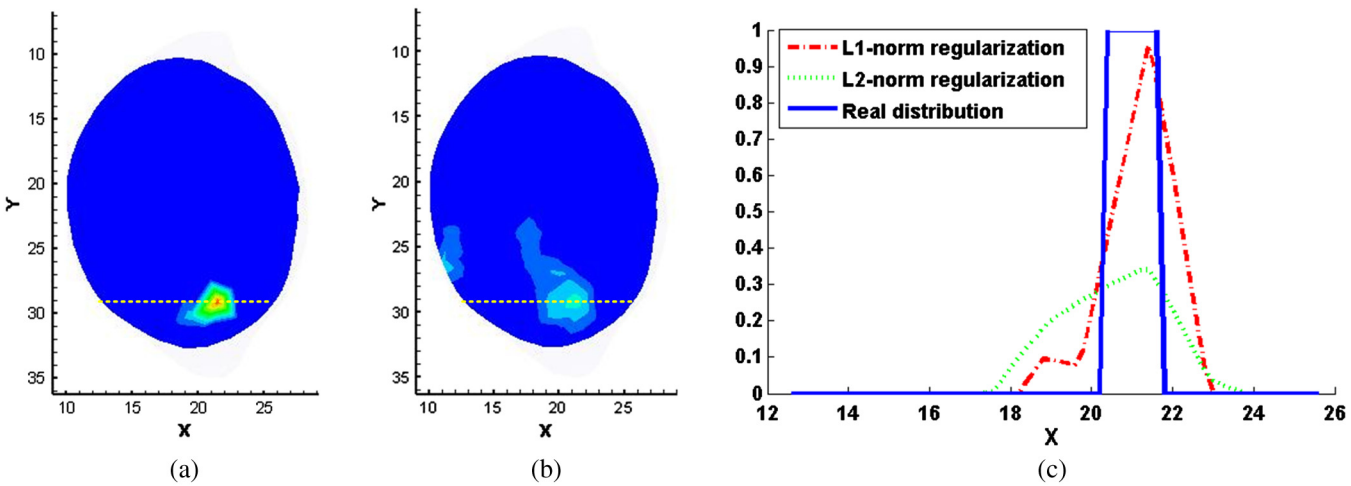

Fig. 7 Fluorescent yield profiles of *in vivo* experiment for model A. The blue solid line of (c) is the real distribution along the yellow dotted lines of (a), while the red dash dot line and green dotted line represent the reconstructed distribution by l_1-norm and l_2-norm regularization methods, respectively.

Table 5 Comparative results for *in vivo* experiment of model A.

Method	Real position center (mm)	Reconstructed position center (mm)	Location error (mm)	Reconstructed fluorescent yield (mm^{-1})	Relative error of yield (%)	Real FWHM (mm)	Reconstructed FWHM (mm)
l_1-norm	(21.1, 27.8, 7.4)	(21.4, 29.1, 8.5)	1.73	0.031	22.5	1.2	1.4
l_2-norm		(20.2, 29.2, 8.6)	2.05	0.011	72.5		3.4

Table 6 Reconstruction results with optical properties perturbation for *in vivo* experiment of model A.

Perturbation	Method	Location error (mm)	Reconstructed fluorescent yield (mm^{-1})
±5%	l_1-norm	1.98 ± 0.14	0.0306 ± 0.0021
	l_2-norm	2.71 ± 1.95	0.0112 ± 0.0002
±10%	l_1-norm	2.40 ± 1.27	0.0307 ± 0.0026
	l_2-norm	4.13 ± 3.03	0.0114 ± 0.0005
±15%	l_1-norm	2.79 ± 1.62	0.0309 ± 0.0037
	l_2-norm	4.12 ± 3.05	0.0116 ± 0.0009

of fluorescent yield is also considered to analyze the results by the following formula:

$$\mathrm{RE} = |Y_r - Y_a|/Y_a, \tag{7}$$

where Y_r is the reconstructed fluorescent yield and Y_a is the actual one. Table 2 gives the comparative results of these two regularization methods according to LE, RE of fluorescent yield, and the full width at half maximum (FWHM). For case 2, the recovered results at coronal and sagittal views are shown in Fig. 5. It is clear that the solution of l_1-norm regularization is concentrated on a localized region, as depicted in Figs. 4(b), 4(f), 4(j), 5(a), and 5(d). However, the solution of l_2-norm regularization has a large area than that of l_1-norm regularization, as shown in Figs. 4(c), 4(g), 4(k), 5(b), and 5(e). In Table 2, the LEs of l_1-norm regularization under the three cases are less than 1 mm, which are smaller than that of

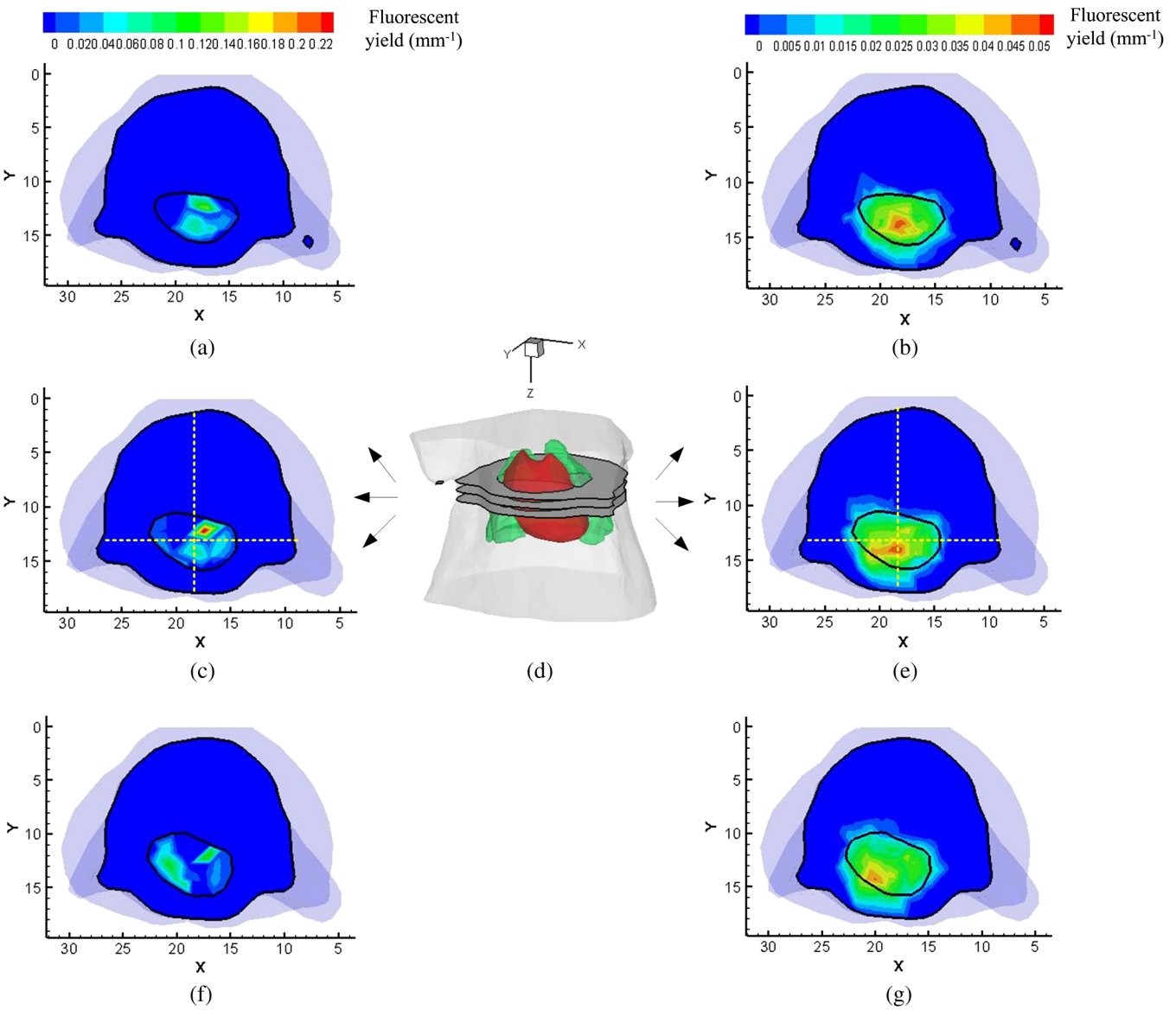

Fig. 8 Reconstruction results of two regularization methods for model B. (a), (c), and (f) are the results at slices $z = 5.5$, 6.5, and 7.5 mm, respectively, by l_1-norm regularization. (b), (e), and (g) are the corresponding results by l_2-norm regularization method. The black contour is the boundary of heart. (d) 3-D view of the three slices.

l_2-norm regularization. In addition, the fluorescent yields of l_1-norm regularization for three cases are 0.050, 0.055, and 0.054 mm^{-1}, respectively, with all REs less than 20%. In contrast, l_2-norm provides results with larger REs of the fluorescent yield. The FWHMs by l_1-norm are less than 2.5 mm, while the ones by l_2-norm are larger than 3 mm, which are greater than the actual value of 2 mm. It means l_1-norm provides a solution confined in a localized region. The last column of Table 2 displays the reconstruction time of l_1-norm and l_2-norm regularization methods. It is obvious that l_2-norm regularization consumed less time than l_1-norm regularization as it was solved by conjugate gradient method. It should be noted that the recovered fluorescent yield values are small than the actual ones. This may be caused by the absence of *a priori* knowledge. For quantitative fluorescence tomography, Lin et al. showed that the true fluorophore concentration could be recovered when both functional optical background and structural *a priori* information, including the location of the fluorophore, are utilized to guide the FMT reconstruction algorithm.[37] In practical applications, the location of the fluorescent target is usually unknown. Our experiments were conducted on this assumption.

The influence of the optical parameters for the reconstruction has been investigated in this paper. We studied the robustness of these two regularization methods against inaccurate optical parameters by adding different perturbation levels (±5%, ±10%, ±15%) to absorption and reduced scattering coefficients at both excitation and emission wavelengths. The perturbation is added by the following formula:

$$\bar{E} = E + \delta \mathrm{PE}, \tag{8}$$

where E is the optical parameters in Table 1 or Table 3, namely μ_{ax}, μ'_{sx}, μ_{am}, or, $\mu'_{sm}\delta$ is the perturbation level parameter, and it is set to 5%, 10%, and 15% in this paper. P is a random number generated by a MATLAB function rand with $P = 2 * \mathrm{rand} - 1$. We carried out 100 independent reconstructions for each perturbation level. The reconstructed results in Table 4 are the average of 100 independent reconstructions. It is obvious that the LE becomes large with the increase of the perturbation levels of optical parameters for both the regularization methods, while the recovered fluorescent yield almost has no change.

Table 7 Full width at half maximum of simulation experiment for model B.

	Method	Real FWHM (mm)	Reconstructed FWHM (mm)
Horizontal lines	l_1-norm	7.8	1
	l_2-norm		7.2
Vertical lines	l_1-norm	5.0	1.2
	l_2-norm		3.4

We have also found that the standard deviations of LE and fluorescent yield by both methods increase with the raise of the perturbation levels. It indicates that the reconstruction results will become more unstable with the increase of perturbation levels.

3.1.2 *In vivo implanted fluorophore experiment*

All animal studies were performed in accordance with the Fourth Military Medical University Guide for the Care and Use of Laboratory Animals formulated by the National Society for Medical Research. An *in vivo* implantation experiment was performed on an adult BALB/C. A glass tube with 0.6 mm radius and 2.8 mm height, which contains Cy5.5 solution (with the extinction coefficient of about 0.019 $mm^{-1}\,\mu M^{-1}$ and quantum efficiency of 0.23 at the peak excitation wavelength of 671 nm),[38] was implanted into the abdomen of the mouse that was anesthetized beforehand. The glass tube, with Cy5.5 (Fanbo, Beijing, China) solution at a concentration of 4000 nM, is the small fluorophore to be recovered. The actual fluorescent yield of Cy5.5 is 0.0402 mm^{-1} according to published literature.[39] The experimental data were acquired by the dual-modality FMT/micro-CT system (see Fig. 2). After the optical image acquisition, the anesthetized mouse was scanned by micro-CT. The CT slices were segmented into major anatomical components, including heart, lungs, liver, kidneys, and muscle. The optical

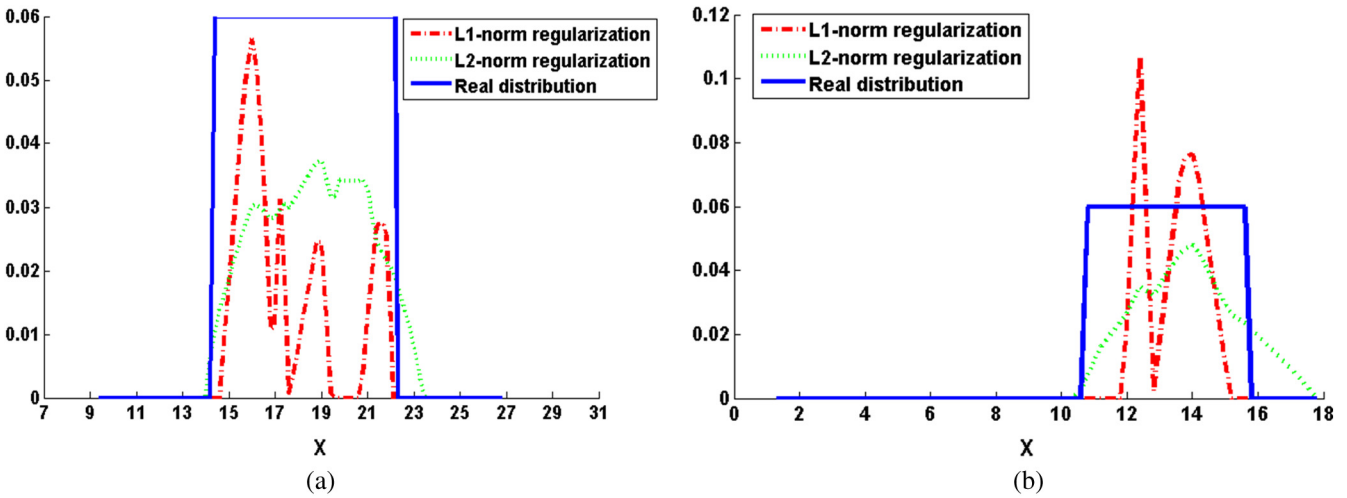

Fig. 9 Fluorescent yield profiles along the yellow dashed lines of Fig. 8. (a) Profiles along the horizontal yellow dashed lines. (b) Profiles along the vertical yellow dashed lines. The blue solid lines are the real distribution along the yellow dotted lines. The red dash dot line and green dotted line represent the reconstructed distribution by l_1-norm and l_2-norm regularization.

properties at both the excitation and emission wavelengths for the main organs were calculated based on the literature as listed in Table 3.[35] A landmarks-based rigid-body registration method was adopted to make the CT data registered with the fluorescence imaging.[33] After the registration, the absolute irradiance distribution in two-dimensional (2-D) fluorescence images was mapped on the 3-D mouse surface.[40] The segmented mouse torso was discretized into 18,504 tetrahedral-elements and 3823 nodes for reconstruction. Figure 6 shows the results by l_1-norm and l_2-norm regularization methods, which are compared with the corresponding CT slices. The recovered center deviation is 1.73 mm using l_1-norm regularization, while using l_2-norm regularization method, the recovered center deviation is 2.05 mm. Figure 7 provides the fluorescent yield profiles of *in vivo* experiment and Table 5 provides the quantitative results. From Figs. 6 and 7, it is clear that the solution of l_1-norm regularization is still confined in a small region with clean background, while the one of l_2-norm regularization has a large area, which is consistent with the numerical experiment results. Furthermore, l_2-norm regularization generated spurious small elements in Fig. 6(b), which also appear in Fig. 4(c) and 4(k). The green solid lines in the longitudinal of Fig. 6(a) are closer to the red dashed lines than that of Fig. 6(b), which indicates that l_1-norm regularization provides a better location of fluorophore than l_2-norm regularization method does.

The optical parameters for the main organs are calculated according to literature,[35] not experimentally measured. However, the tissue optical parameters of the mouse in our experiments may be significantly different from the literature data. So we have also studied the influence by changing the optical parameters for reconstruction. Table 6 provides the quantitative analysis for each perturbation level. From Table 6, we have found that the LE by two methods increases with the raise of the perturbation levels of optical parameters, while the recovered fluorescent yield increases slightly. It is clear

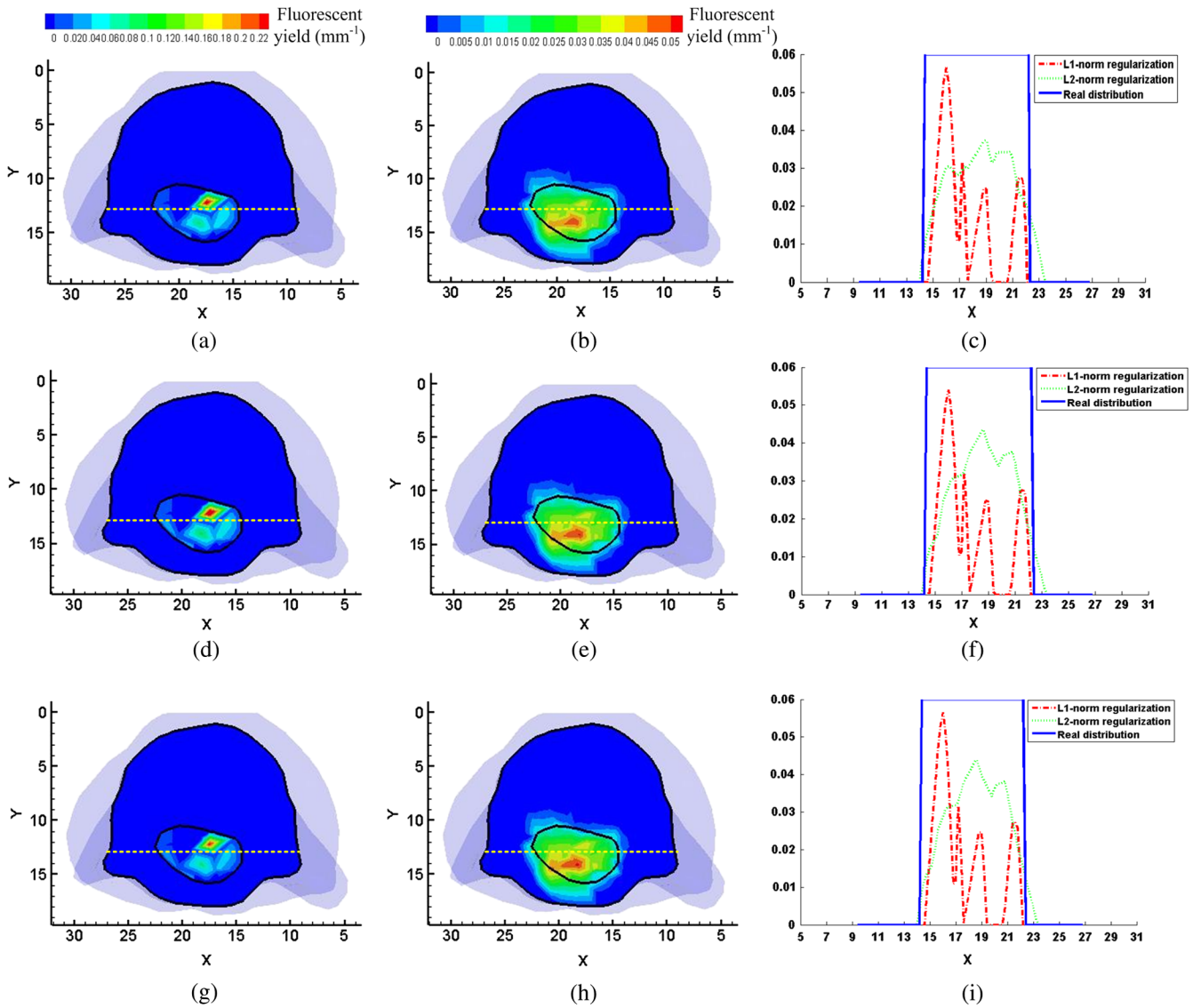

Fig. 10 Results of simulation experiments for model B with optical parameters perturbation at ±5%, ±10%, and ±15%. The first column is recovered by l_1-norm regularization, and the second column is reconstructed by l_2-norm regularization. The third column is the profiles along the yellow dotted lines in the first and second columns. The blue solid lines are the real distribution along the yellow dotted lines. The red dash dot line and green dotted line represent the reconstructed distribution by l_1-norm and l_2-norm regularization.

Table 8 Average fluorescent yield in the organ for simulation experiment and *in vivo* experiment of model B.

		Simulation experiments	In vivo experiments
Perturbation	Method	Average fluorescent yield (mm^{-1})	Average fluorescent yield (mm^{-1})
0	l_1-norm	0.0207 ± 0	0.0022 ± 0
	l_2-norm	0.0216 ± 0	0.0033 ± 0
±5%	l_1-norm	0.0220 ± 0.0006	0.0022 ± 0.0003
	l_2-norm	0.0222 ± 0.0005	0.0032 ± 0.0002
±10%	l_1-norm	0.0219 ± 0.0009	0.0022 ± 0.0006
	l_2-norm	0.0224 ± 0.0013	0.0032 ± 0.0004
±15%	l_1-norm	0.0221 ± 0.0017	0.0022 ± 0.0009
	l_2-norm	0.0224 ± 0.0014	0.0033 ± 0.0005

that the standard deviation increases with the raise of the perturbation levels, which indicates that the reconstruction results are very unstable when the perturbation level of optical parameters is large. This conclusion is consistent with the numerical experiment.

3.2 *Model B: Reconstruction of Fluorescent Dye Distribution in Organs*

3.2.1 *Numerical simulation*

In the numerical experiment, the mouse chest region is considered instead of the torso section, as shown in Fig. 1(b). The heart was considered as an entirety, and the atriums, ventricles, and vessels were not considered. Our aim was to recover the fluorophore distribution in the heart. The fluorescence yield was set to be 0.06 mm^{-1}. The optical parameters for major organs are shown in Table 1. A coarse mesh (2292 nodes and 11,737 tetrahedral-elements) was used for the inverse problem. Figure 8 presents the recovered results by l_1-norm and l_2-norm regularization methods. For clarification, we display the results at slices $z = 5.5$, 6.5, and 7.5 mm, respectively. It seems that the solution of l_1-norm regularization is confined in small regions. On the

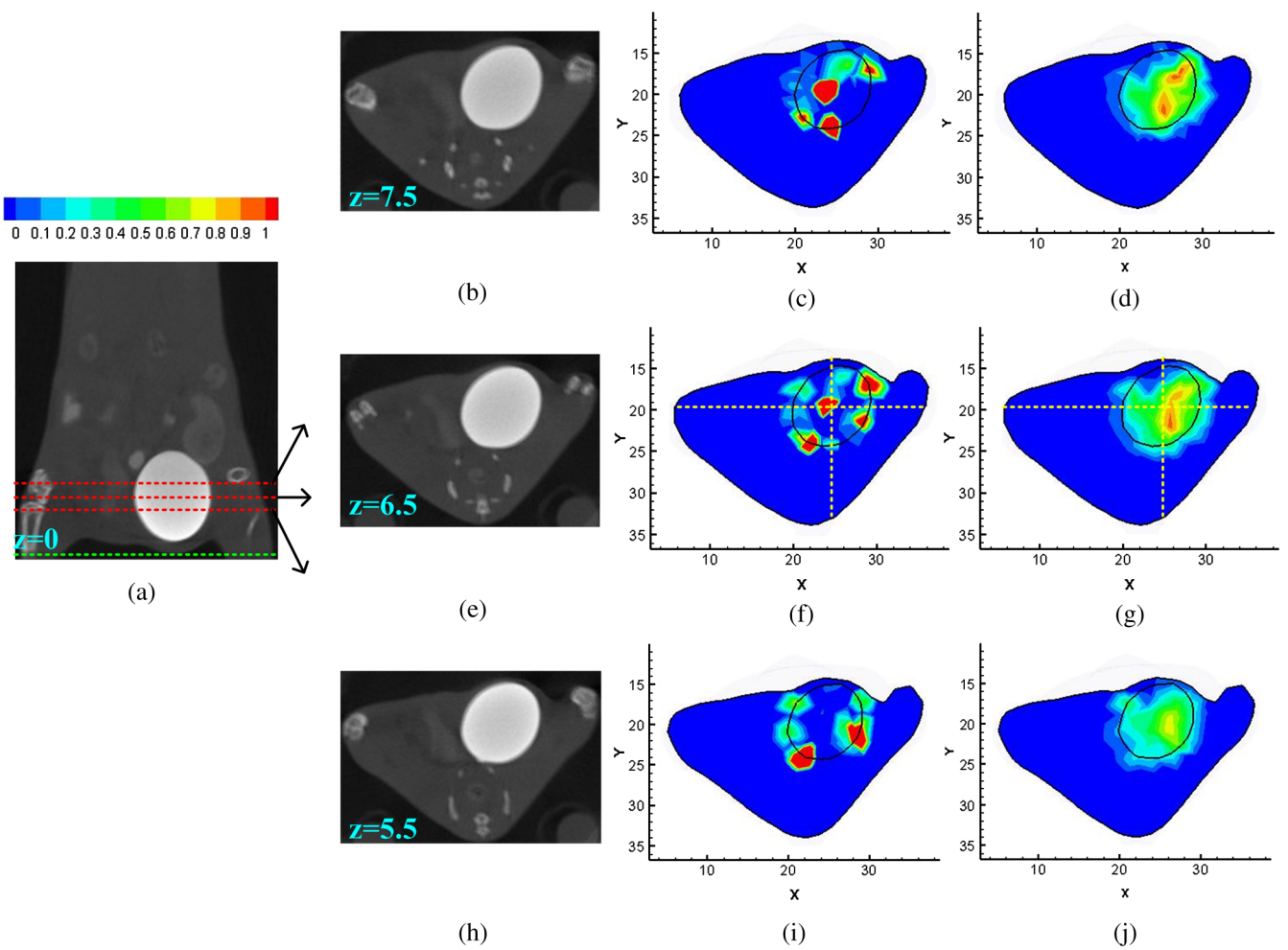

Fig. 11 Results of reconstruction of Cy5.5 solution in the bladder of the mouse by l_1-norm and l_2-norm regularization methods. The reconstructed images are normalized by the maximum value of l_2-norm. (a) XCT coronal slice. The red dot lines represent the positions of investigated slices. (c), (f), and (i) are the results by l_1-norm and (d), (g), and (j) by l_2-norm regularization method.

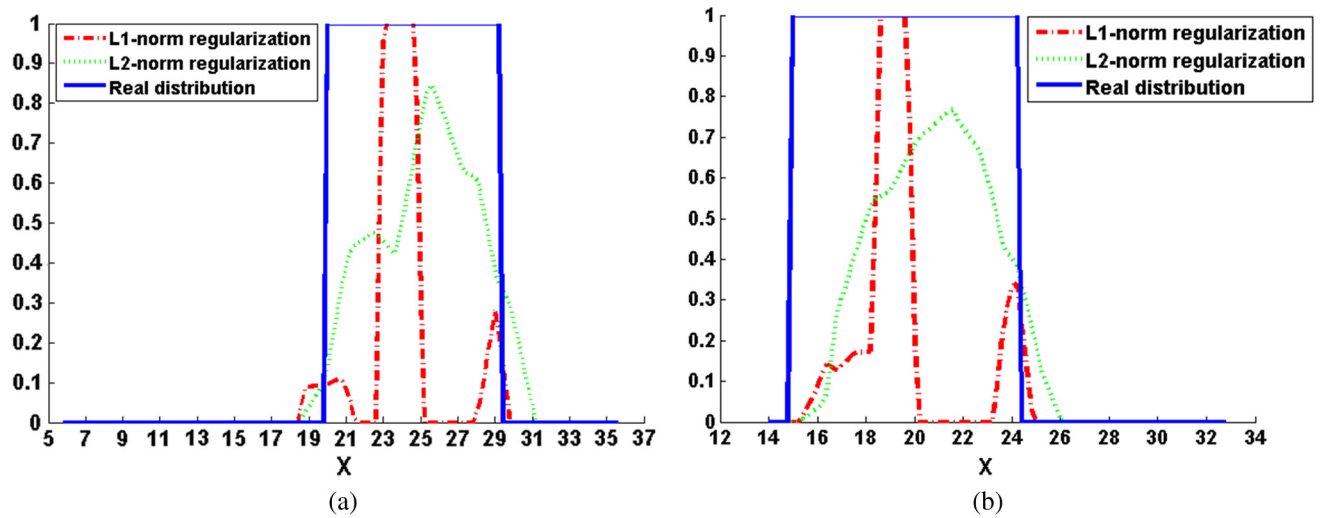

Fig. 12 Profiles along the yellow dashed lines of Fig. 11. (a) Profiles along the horizontal yellow dashed lines. (b) Profiles along the vertical yellow dashed lines. The blue solid lines are the real distribution along the yellow dotted lines. The red dash dot line and green dotted line represent the reconstructed distribution by l_1-norm and l_2-norm regularization.

contrary, the solution of l_2-norm is smooth and has a large area. This indicates that l_1-norm regularization still provides a solution with a localized region, while l_2-norm regularization gives a reasonable solution. This is because l_1-norm regularization tends to find sparse solutions, while l_2-norm regularization tends to penalize large elements. The profiles along the yellow dotted lines in Fig. 8 are shown in Fig. 9. Figure 9(a) is a profile of horizontal lines and Fig. 9(b) is one of vertical lines. Table 7 provides the FWHM for simulation experiments of model B. From Fig. 9 and Table 7, the FWHM of either horizontal or vertical lines, it is clear that the FWHM of l_2-norm is much closer to the actual FWHM. It means the solution provided by l_2-norm has large volume and is more approximated to the actual one.

We have also investigated the influence by changing optical parameters on the recovered results for model B. Figure 10 shows the recovered results for perturbation levels at ±5%, ±10%, and ±15%. The third column is the profiles along the yellow dotted lines in the first and second columns. The blue solid lines are the real distribution along the yellow dotted lines. The red dashed lines and green solid lines represent the reconstructed distribution by l_1-norm and l_2-norm regularization. There is a slight variation in the distribution, as shown in Fig. 10(c), 10(f), and 10(i). In order to show the reconstruction results clearly, we have introduced the average fluorescent yield, which is the ratio of total fluorescent yield to the total volume of the organ. The average fluorescent yields of the heart by two methods for each perturbation level are shown in the third column of Table 8. There is little variation in the average fluorescent yield by the two methods, but the standard deviations of average fluorescent yield increase with the increase of perturbation levels.

3.2.2 *Reconstruction of Cy5.5 solution distribution in the bladder of mouse*

The Cy5.5 solution of 0.12 ml, with a concentration of 4000 nM, was injected to an adult BALB/C mouse via tail vein. We considered the lower body of the mouse as the reconstruction region, and the problem was to recover the distribution of Cy5.5 in the bladder. After 6 h, we acquired the data using our prototype FMT/micro-CT dual-modality imaging system for reconstruction. The optical properties of main organs are listed in Table 3. The segmented mouse torso was discretized into 14,500 tetrahedral-elements and 3085 nodes for reconstruction. The actual concentration of Cy5.5 in the bladder is unknown, and the recovered results are normalized by the maximum value of l_2-norm for comparison. Figure 11 shows the results, which are compared to the corresponding CT slices. It is clear that the solution of l_1-norm regularization concentrates on some small regions, while the solution of l_2-norm regularization has a large area and is smooth, which are consistent with the results in the numerical experiments. Figure 12 is profiles along the yellow dotted lines in Fig. 11, and Table 9 is the FWHM of *in vivo* experiment.

Figure 13 shows the reconstructed results under the optical parameters perturbation at 0, ±5%, ±10%, and ±15%. All of the results are normalized by the maximum value recovered by l_2-norm regularization with no optical properties perturbation. The third column is the profiles along the yellow dotted lines in the first and second columns. The blue solid lines are the real distributions along the yellow dotted lines. The red dash-dot lines and green solid lines represent the reconstructed distribution by l_1-norm and l_2-norm regularization. The first row is results with no optical parameters perturbation, and the second row is for perturbation at ±5%, the third row is for ±10%, and

Table 9 Full width at half maximum of *in vivo* experiment for model B.

	Method	Real FWHM (mm)	Reconstructed FWHM (mm)
Horizontal lines	l_1-norm	9.2	1.4
	l_2-norm		6.0
Vertical lines	l_1-norm	9.4	2.0
	l_2-norm		7.0

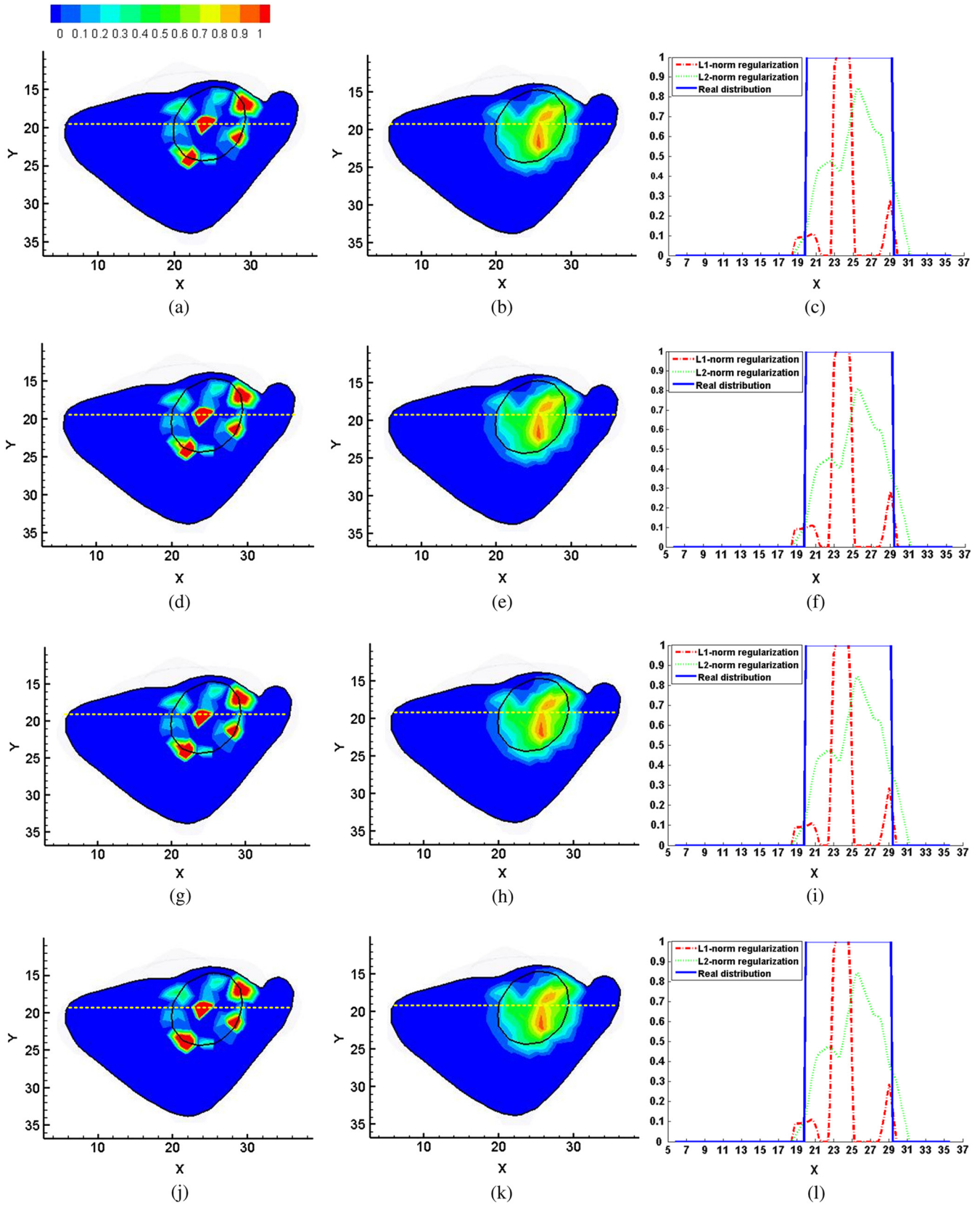

Fig. 13 The recovered results for *in vivo* experiments of model B with optical parameters perturbation at 0, ±5%, ±10%, and ±15%. All of the results are normalized by the maximum value recovered by l_2-norm regularization with no perturbation. The first row is the results with no perturbation, the second row is for ±5%, the third row is for ±10%, and the fourth row is for ±15%. The first column is reconstructed by l_1-norm regularization and the second column by l_2-norm regularization. The third column is the profiles along the yellow dotted lines in the first and second column. The blue solid lines are the real distribution along the yellow dotted lines. The red dash dot line and green dotted line represent the reconstructed distribution by l_1-norm and l_2-norm regularization.

the fourth row is for ±15%. The average fluorescent yield of the bladder is shown in the fourth column of Table 8. We have found that there is almost no change in the average value, but the standard deviations of average fluorescent yield by two methods increase with the raise of perturbation levels.

4 Discussion and Conclusion

In this paper, we make a comprehensive comparison between l_1-norm and l_2-norm regularization methods based on two imaging models of FMT. For the early detection of tumor model, numerical experiments and *in vivo* experiments were conducted to test the two methods. The experiment results indicate that l_1-norm regularization produced the solution confined in a localized region with clean background, while l_2-norm regularization created a smooth solution with a large volume and generated spurious small elements. It should be noted that the recovered LEs of *in vivo* experiment were larger than that of the numerical experiments. This may be caused by many factors: (1) the photon propagation was described by diffusion approximation, not the radiative transfer equation,[41] (2) the optical properties for major organs were using the published values, not using DOT,[7,9] (3) experimental operations may also affect the reconstruction results. In the model of reconstructing the distribution of fluorescent dye in organs, l_1-norm regularization shrunk the support of the fluorescent and still provided the solution with small volume, while l_2-norm regularization produced a smooth solution with a large volume. The FWHM of fluorescent yield profiles by l_2-norm is more close to the actual one than that of l_1-norm. We infer that for these two imaging models of FMT, the l_1-norm regularization is a more suitable choice for the reconstruction of small fluorophore as it fully takes advantage of the sparse characteristic of the fluorophore; l_2-norm regularization is more accurate for reconstructing the distribution of fluorescent dye in organs since it tends to penalize large elements.

It should be noted that the size and shape of fluorescent target cannot be accurately recovered by either l_1-norm or l_2-norm regularization. It is desirable to design more appropriate regularization methods for this problem. Gao et al. have developed total variation and l_1 data fidelity for bioluminescence tomography based on radiative transfer equation. [42] This algorithm showed good performance for 2-D numerical simulation experiments, especially on preserving the boundary of the object. The extensive clinical applications could encounter difficulties for the complex 3-D reconstruction. This is our future research.

In conclusion, we have made a detailed comparison between l_1-norm and l_2-norm regularization methods based on two imaging models of FMT. Some interesting conclusions were obtained in this paper, which would provide useful information for the researcher in selecting and designing algorithms for FMT reconstruction.

Acknowledgments

This work was supported by the Program of the National Basic Research and Development Program of China (973) under Grant No. 2011CB707702, the National Natural Science Foundation of China under Grant Nos. 81090270, 81090272, 81227901, 81000632, 81101084, the National Key Technology Support Program under Grant No. 2012BAI23B06, and the Fundamental Research Funds for the Central Universities.

References

1. V. Ntziachristos et al., "Looking and listening to light: the evolution of whole body photonic imaging," *Nat. Biotechnol.* **23**(3), 313–320 (2005).
2. E. E. Graves, R. Weissleder, and V. Ntziachristos, "Fluorescence molecular imaging of small animal tumor models," *Curr. Mol. Med.* **4**(4), 419–430 (2004).
3. A. Corlu et al., "Three-dimensional *in vivo* fluorescence diffuse optical tomography of breast cancer in humans," *Opt. Express* **15**(11), 6696–6716 (2007).
4. M. J. Niedre et al., "Early photon tomography allows fluorescence detection of lung carcinomas and disease progression in mice *in vivo*," *Proc. Nat. Acad. Sci. U.S.A.* **105**(49), 19126–19131 (2008).
5. J. K. Willmann et al., "Molecular imaging in drug development," *Nat. Rev. Drug Discov.* **7**(7), 591–607 (2008).
6. R. B. Schulz et al., "Hybrid system for simultaneous fluorescence and x-ray computed tomography," *IEEE Trans. Med. Imag.* **29**(2), 465–473 (2010).
7. Y. Lin et al., "Quantitative fluorescence tomography using a combined tri-modality FT/DOT/XCT system," *Opt. Express* **18**(8), 7835–7850 (2010).
8. F. Stuker et al., "Hybrid small animal imaging system combining magnetic resonance imaging with fluorescence tomography using single photon avalanche diode detectors," *IEEE Trans. Med. Imag.* **30**(6), 1265–1273 (2011).
9. Y. Tan and H. Jiang, "DOT guided fluorescence molecular tomography of arbitrarily shaped objects," *Med. Phys.* **35**(12), 5703–5707 (2008).
10. X. Zhang, C. T. Badea, and G. A. Johnson, "Three-dimensional reconstruction in free-space whole-body fluorescence tomography of mice using optically reconstructed surface and atlas anatomy," *J. Biomed. Opt.* **14**(6), 064010 (2009).
11. A. D. Zacharopoulos et al., "A matrix-free algorithm for multiple wavelength fluorescence tomography," *Opt. Express* **17**(5), 3025–3035 (2009).
12. D. Han et al., "Sparsity promoting tomographic fluorescence imaging with simplified spherical harmonics approximation," *IEEE Trans. Biomed. Eng.* **57**(10), 2564–2567 (2010).
13. P. Mohajerani et al., "Optimal sparse solution for fluorescent diffuse optical tomography: theory and phantom experimental results," *Appl. Opt.* **46**(10), 1679–1685 (2007).
14. B. Alacam and B. Yazici, "Direct reconstruction of pharmacokinetic-rate images of optical fluorophores from NIR measurements," *IEEE Trans. Med. Imag.* **28**(9), 1337–1353 (2009).
15. V. V. Tuchin, "Light scattering studies of tissues," *Phys. Usp.* **40**(5), 495–515 (1997).
16. S. R. Arridge, "Optical tomography in medical imaging," *Inverse Probl.* **15**(2), R41–R93 (1999).
17. A. Kienle and M. S. Patterson, "Improved solutions of the steady-state and the time-resolved diffusion equations for reflectance from a semi-infinite turbid medium," *J. Opt. Soc. Am. A.* **14**(1), 246–254 (1997).
18. M. Schweiger et al., "The finite element method for the propagation of light in scattering media: boundary and source conditions," *Med. Phys.* **22**(11), 1779–1792 (1995).
19. S. R. Arridge et al., "A finite element approach for modeling photon transport in tissue," *Med. Phys.* **20**(2), 299–309 (1993).
20. M. Schweiger, S. R. Arridge, and D. T. Delpy, "Application of the finite-element method for the forward and inverse models in optical tomography," *J. Math. Imag. Vis.* **3**(3), 263–283 (1993).
21. D. Wang et al., "A novel finite-element-based algorithm for fluorescence molecular tomography of heterogeneous media," *IEEE Trans. Inf. Technol. Biomed.* **13**(5), 766–773 (2009).
22. W. Sun and Y. Yuan, *Optimization Theory and Method*, Springer, New York (2006).
23. M. Kojima, N. Megiddo, and S. Mizuno, "Theoretical convergence of large-step primal-dual interior point algorithms for linear programming," *Math. Program.* **59**(1–3), 1–21 (1993).
24. G. Davis, S. Mallat, and M. Avellaneda, "Adaptive greedy approximations," *Constr. Approx.* **13**(1), 57–98 (1997).
25. I. Daubechies, M. Defrise, and C. Mol, "An iterative thresholding algorithm for linear inverse problems with a sparsity constraint," *Commun. Pure Appl. Math.* **57**(11), 1413–1457 (2004).

26. R. Etzioni et al., "The case for early detection," *Nat. Rev. Cancer* **3**(4), 243–252 (2003).
27. R. Ellman et al., "Breast self-examination programmes in the trial of early detection of breast cancer: ten years findings," *Br. J. Cancer* **68**(1), 208–212 (1993).
28. P. Cairns, "Gene methylation and early detection of genitourinary cancer: the road ahead," *Nat. Rev. Cancer* **7**(7), 531–543 (2007).
29. A. McWilliams et al., "Innovative molecular and imaging approaches for the detection of lung cancer and its precursor lesions," *Oncogene* **21**(45), 6949–6959 (2002).
30. A. Levin and P. E. Stevens, "Early detection of CKD: the benefits limitations and effects on prognosis," *Nat. Rev. Nephrol.* **7**(8), 446–457 (2011).
31. A. Herbst et al., "Methylation of NEUROG1 in serum is a sensitive marker of the detection of early colorectal cancer," *Am. J. Gastroenterol.* **106**(6), 1110–1118 (2011).
32. G. Yan et al., "Fast cone-beam CT image reconstruction using GPU hardware," *J. X-Ray Sci. Technol.* **16**(4), 225–234 (2008).
33. X. He et al., "Sparse reconstruction for quantitative bioluminescence tomography based on the incomplete variables truncated conjugate gradient method," *Opt. Express* **18**(24), 24825–24841 (2010).
34. B. Dogdas et al., "Digimouse: a 3D whole body mouse atlas from CT and cryosection data," *Phys. Med. Biol.* **52**(3), 577–587 (2007).
35. G. Alexandrakis, F. R. Rannou, and A. F. Chatziioannou, "Tomographic bioluminescence imaging by use of a combined optical-PET (OPET) system: a computer simulation feasibility study," *Phys. Med. Biol.* **50**(17), 4225–4241 (2005).
36. A. Cong and G. Wang, "A finite-element-based reconstruction method for 3D fluorescence tomography," *Opt. Express* **13**(24), 9847–9857 (2005).
37. Y. Lin et al., "Quantitative fluorescence tomography using a trimodality system: *in vivo* validation," *J. Biomed. Opt.* **15**(4), 040503 (2010).
38. F. Gao et al., "A linear, featured-data scheme for image reconstruction in time-domain fluorescence molecular tomography," *Opt. Express* **14**(16), 7109–7124 (2006).
39. M. A. Naser and M. S. Patterson, "Improved bioluminescence and fluorescence reconstruction algorithms using diffuse optical tomography, normalized data, and optimized selection of the permissible source region," *Biomed. Opt. Express* **2**(1), 169–184 (2011).
40. X. Chen et al., "3D reconstruction of light flux distribution on arbitrary surfaces from 2D multi-photographic images," *Opt. Express* **18**(19), 19876–19893 (2010).
41. Y. Lu et al., "Experimental bioluminescence tomography with fully parallel radiative-transfer-based reconstruction framework," *Opt. Express* **17**(19), 16681–16695 (2009).
42. H. Gao and H. Zhao, "Multilevel bioluminescence tomography based on radiative transfer equation. Part 2: total variation and l_1 data fidelity," *Opt. Express* **18**(3), 2894–2912 (2010).